Pressure-swirl atomization: Modeling and experimental approaches

Abdelhak Belhadef, Ariane Vallet, Muriel Amielh, Fabien Anselmet

Pressure-swirl atomization: Modeling and experimental approaches

A. Belhadef [a,*], A. Vallet [a], M. Amielh [b], F. Anselmet [b]

[a] CEMAGREF, UMR ITAP, 361 rue J.F. Breton, 34196 Montpellier, France
[b] Aix-Marseille Univ., CNRS, IRPHE, UMR 6594, 13384 Marseille, France

An Eulerian model is developed to model liquid sheet atomization with high Weber and Reynolds numbers. The model considers a single phase of liquid–gas mixture to represent the turbulent mixing of the liquid sheet with the ambient gas. As the flow is highly swirled and highly anisotropic, the Reynolds stress model is used for turbulence. The turbulent flux of liquid mass fraction is modeled taking into account density variation effect. The mean liquid–gas interface density balance equation is solved to get the Sauter Mean Diameter of droplets. 2-D axisymmetric swirl calculations have been performed using 3-D results as boundary conditions in order to reduce the computational time. Experimental data are obtained using Phase Doppler Anemometry (PDA). Atomization characteristics such as the axial velocity and droplet Sauter Mean Diameter were determined experimentally and were compared with the modeling results. Agreement between predictions and measurements is reasonably good.

1. Introduction

The aim of the present study is to propose a model in order to describe and compute the atomization of the pressure-swirl atomizer. Limiting droplet drift during the pulverization depends, in particular, on droplet size and velocity at nozzle exit. Small droplets lead to an optimal coverage but may contribute to drift contaminating air, water and soils. Large droplets are less prone to drift but may stream down. Slow droplets can be carried by the mass of air or fall to the ground before reaching the target. The droplets having a significant kinetic energy will tend to rebound off the leaves. However, the size and the velocity of the droplets depend mainly on the nozzle itself and injection characteristics. The pressure-swirl nozzle is one of the most commonly used type in orchards and vineyards (Melese Endalew et al., 2010). The flow is first introduced axially through inlet ports. It then goes tangentially through tangential channels into a swirl chamber. Finally, the flow is accelerated in the axial direction in order to pass through the discharge hole exit into the ambient air. The tangential channels have spirally shaped grooves and generate a rotating flow. Axial and swirl velocity components depend on these tangential channels (Nonnenmacher and Piesche, 2000). The swirl chamber length has not effect on the spray. Sheet shape and velocity are at most very weakly related to this parameter, since, the swirl strength decreases in the case of smaller chamber radius and causes the reduction of the cone angle and core radius (Park and Heister, 2006).

During past years, many experimental and theoretical studies have been carried out to examine pressure-swirl atomization. The most comprehensive theoretical treatment of the problem is that of Ponstein (1959). Study of the swirl effect on the atomization of a liquid sheet has been performed by Rho et al. (1998). Rizk and Lefebvre (1985) studied the impact of certain geometrical dimensions of swirl nozzles on the sprays produced.

The liquid is injected at very high velocity so that the liquid sheet undergoes instabilities linked in particular to the large slip velocity between the liquid sheet and ambient air, density gradient and turbulence. This instability causes the liquid sheet break-up into ligaments which then break-up into droplets. The resulting liquid sheet rotates, the air core region is forced to rotate by the shear layer attached to the liquid sheet and the forced air vortex induces low pressure region which causes back flow at the center line of the spray in what is called a recirculation vortex (Chigier and Beer, 1964 and Moona et al., 2009).

The resulting liquid sheet at the nozzle outlet widens in the form of the cone after leaving the nozzle and disintegrates downstream into droplets (Nonnenmacher and Piesche, 2000). The larger droplets move along with their original flight angles and can penetrate the outer lateral regions of the spray. The smaller droplets are mostly confined in the core regions of the spray

* Corresponding author. Tel.: +33 6 28 57 03 62; fax: +33 4 67 04 63 06.
E-mail address: a.belhadef@gmail.com (A. Belhadef).

(Chang et al., 1993 and Yang et al., 2003). The small droplets inside the core vortex are carried backward by the air flow. The droplet size decreases when increasing swirl velocity (Park et al., 2006).

Several approaches are used to investigate atomization. There are among others interface tracking methods, like Volume Of Fluid (VOF, Hirt and Nichols, 1981) and Level-Set. VOF focuses on the computation of the fluid volume at each cell. Reconstruction algorithms are used to build numerical flux by geometrical considerations ensuring local conservation of mass. However, these reconstruction algorithms are very complex and costly in terms of computation time and the passage of a two-dimensional to three-dimensional calculation is not immediate because the reconstruction geometry of interface is not the same. Level-Set method (Osher and Sethian, 1988) is based on a signed distance function continuously and sufficiently regular at the interface who is advected by the flow. Level-Set method requires the use of an algorithm and this algorithm leads to mass loss by moving of artificial interface enhancing numerical diffusion.

Moreover, in Computational Fluid Dynamics, two phase flows are commonly modeled using two different approaches: the Eulerian method, where the spray is considered as a continuum across the whole flow domain, and the Lagrangian method, where the paths taken by droplets are tracked through the domain. A combination of an Eulerian k–ϵ turbulence model, to describe the interaction between droplets and gas phase in the secondary breakup, with a lagrangian method, to model the disperse droplet phase, is achieved by Lin et al. (2009) and Xiong et al. (2009) in a (non-swirling) effervescent atomization spray. In these related works, the droplet velocity is finally calculated in the spray far field by a one-phase model initially developed for variable density jets.

Within Eulerian methods, the two-fluid model (Ishii, 1975 and Drew, 1983) solves state equation for each fluid and takes into account interactions between phases. Drawbacks of this method include interfacial terms complex modeling and the high number of equations as each fluid is transported. On the other hand, the one-fluid Eulerian model used in this study has the advantage to compute only the transport of one single fluid with high density variation.

In the second part of this paper, Eulerian model is presented. The following section focuses on a numerical procedure used to solve equations of the model. The aim of the forth section is to describe the experimental set-up of Phase Doppler Anemometry (PDA) system. Finally, the last section is devoted to modeling results and comparison with experimental results.

2. Eulerian model

An Eulerian one phase model with high Weber and Reynolds numbers (capillarity and molecular viscosity are neglected at large scales) is adapted to compute flow inside and outside an agricultural nozzle (De Luca et al., 2009). The two-phase flow is considered as a single phase turbulent flow composed of a liquid and a gas mixture with a highly variable mean density $\bar{\rho}$. Classical conservation equations for the total mass and the mean momentum of the stationary turbulent flow are considered.

$$\frac{\partial \bar{\rho}\tilde{u}_j}{\partial x_j} = 0 \tag{1}$$

$$\frac{\partial \bar{\rho}\tilde{u}_i\tilde{u}_j}{\partial x_j} = -\frac{\partial \bar{p}}{\partial x_i} - \frac{\partial \bar{\rho}\widetilde{u_i''u_j''}}{\partial x_j} \tag{2}$$

where $\bar{p}$ is the mean pressure, $x_i, \tilde{u}_i$ and u_i'' are the coordinate, Favre averaged velocity component and velocity fluctuation component respectively in the ith direction.

The mean density is related to the Favre averaged liquid mass fraction $\widetilde{Y}$ by:

$$\frac{1}{\bar{\rho}} = \frac{\widetilde{Y}}{\rho_l} + \frac{1-\widetilde{Y}}{\rho_g} \tag{3}$$

where ρ_g and ρ_l are the constant gas and liquid densities respectively.

Liquid mass fraction conservation equation is written as:

$$\frac{\partial(\bar{\rho}\widetilde{Y}\tilde{u}_i)}{\partial x_i} = -\frac{\partial}{\partial x_i}\left(\bar{\rho}\widetilde{u_i''Y''}\right) \tag{4}$$

where $Y'' = Y - \widetilde{Y}$ is the liquid mass fraction fluctuation. RHS term of Eq. (4) consists only of turbulent diffusion term. Evaporation is actually neglected in this study.

The turbulent flux of liquid mass fraction, $\bar{\rho}\widetilde{u_i''Y''}$, is usually modeled by a first order closure based on a gradient law (De Luca et al., 2009; Lebas et al., 2009; Luret et al., 2010)

$$\bar{\rho}\widetilde{u_i''Y''} = -\frac{\mu_t}{Sc_t}\frac{\partial \widetilde{Y}}{\partial x_i} \tag{5}$$

where $Sc_t = 0.7$ is the turbulent Schmidt number, $\mu_t = C_\mu \bar{\rho}\tilde{k}^2/\tilde{\epsilon}$ is the turbulent viscosity, $\tilde{k} = \widetilde{u_i''u_i''}/2$ is the mean turbulent kinetic energy, $\tilde{\epsilon}$ the dissipation rate and $C_\mu = 0.09$.

However, in this type of modeling, the density variation effect is not taken into account explicitly. In this study, we chose to adopt closure which takes into account the density variation effect, considering the large density difference between liquid and gas in the studied flow (Demoulin et al., 2007).

$$\bar{\rho}\widetilde{u_i''Y''} = -\left[\frac{\mu_t}{Sc_t} + \frac{C_p\tilde{k}^2}{\tilde{\epsilon}}\bar{\rho}^2\left(\frac{1}{\rho_g} - \frac{1}{\rho_l}\right)\right]\frac{\partial \widetilde{Y}}{\partial x_i} \tag{6}$$

where $C_p = 0.6$ in this study.

The mean liquid volume fraction $\bar{\tau}$ is obviously linked to the mean mass fraction $\widetilde{Y}$ by:

$$\bar{\tau} = \frac{\bar{\rho}\widetilde{Y}}{\rho_l} \tag{7}$$

As the flow considered is highly swirled and highly anisotropic, the Reynolds Stress Model is used:

$$\frac{\partial\left(\bar{\rho}\widetilde{u_i''u_j''}\tilde{u}_k\right)}{\partial x_k} = \frac{\partial}{\partial x_k}\left(\frac{\mu_t}{\sigma_k}\frac{\partial \widetilde{u_i''u_j''}}{\partial x_k}\right) - \bar{\rho}\widetilde{u_i''u_k''}\frac{\partial \tilde{u}_j}{\partial x_k} - \bar{\rho}\widetilde{u_j''u_k''}\frac{\partial \tilde{u}_i}{\partial x_k} + \Phi_{ij} - \frac{2}{3}\bar{\rho}\tilde{\epsilon}\delta_{ij} \tag{8}$$

where $\sigma_k = 0.82$.

The pressure strain term Φ_{ij} represents the energy redistribution on the normal components of the Reynolds tensor and is modeled according to Gibson and Launder (1978) and Fu et al. (1987).

The transport equation for the turbulent dissipation rate $\tilde{\epsilon}$ is given by:

$$\frac{\partial \bar{\rho}\tilde{\epsilon}\tilde{u}_i}{\partial x_i} = \frac{\partial}{\partial x_i}\left(\frac{\mu_t}{\sigma_\epsilon}\frac{\partial \tilde{\epsilon}}{\partial x_i}\right) - C_{\epsilon 1}\bar{\rho}\frac{\tilde{\epsilon}}{\tilde{k}}\widetilde{u_i''u_j''}\left(\frac{\partial \tilde{u}_i}{\partial x_j}\right) - C_{\epsilon 2}\bar{\rho}\frac{\widetilde{\epsilon^2}}{\tilde{k}} \tag{9}$$

where $\sigma_\epsilon = 1.0$, $C_{\epsilon 1} = 1.44$ and $C_{\epsilon 2} = 1.92$ (Launder and Spalding, 1972).

During atomization process, liquid sheet is disintegrated into liquid parcels or blobs that are not necessarily spherical. Liquid parcels are broken up by turbulent stretching and collision events leading to smaller droplets. Moreover, coalescence leads to larger droplets. In order to get the mean droplet length scale, a transport

equation for the mean liquid/gas interface density $\overline{\Sigma}$ is solved (Vallet et al., 2001).

$$\frac{\partial \overline{\Sigma}\tilde{u}_i}{\partial x_i} = \frac{\partial}{\partial x_i}\left(\frac{\mu_t}{\bar{\rho} Sc_\Sigma}\frac{\partial \overline{\Sigma}}{\partial x_i}\right) + (A+a)\overline{\Sigma} - V_a\overline{\Sigma}^2 \tag{10}$$

On the RHS of Eq. (10), the first term concerns the diffusion and Sc_Σ is a constant equal to 0.7. The A term of the second term on the RHS represents the production of the mean interfacial surface by the mean flow stretching and is proportional to the inverse of the characteristic time of turbulent kinetic energy production term:

$$A = -\alpha_0 \frac{\widetilde{u_i'' u_j''}}{\tilde{k}}\frac{\partial \tilde{u}_i}{\partial x_j} \tag{11}$$

where α_0 equals 2.5 in this study.

The a term in Eq. (10) also corresponds to the production of interface and is given by the following expression:

$$a = a_{turb} + a_{coll} \tag{12}$$

This term is composed of two components. The first one a_{turb} represents the production by turbulence and is proportional to the inverse of the turbulence time scale:

$$a_{turb} = \alpha_1 \frac{\tilde{\epsilon}}{\tilde{k}} \tag{13}$$

where α_1 is constant equal to 0.5.

The other one a_{coll} deals with the effect of the droplet break-up due to collisions and is proportional to the inverse of a collision time:

$$a_{coll} = \frac{\alpha_2 C_\mu^{1/2}}{(36\pi)^{2/9}}\tilde{\epsilon}^{1/3}\rho_l^{4/9}\bar{\rho}^{-4/9}\widetilde{Y}^{-4/9}\overline{\Sigma}^{2/3} \tag{14}$$

where α_2 is constant equal to 1.0.

The final expression of the production term a is obtained by summing the two terms a_{turb} and a_{coll}:

$$a = \alpha_1 \frac{\tilde{\epsilon}}{\tilde{k}} + \frac{\alpha_2 C_\mu^{1/2}}{(36\pi)^{2/9}}\tilde{\epsilon}^{1/3}\rho_l^{4/9}\bar{\rho}^{-4/9}\widetilde{Y}^{-4/9}\overline{\Sigma}^{2/3} \tag{15}$$

The last term of Eq. (10) is a destruction term and is related to coalescence droplet effect. Production and destruction terms of Eq. (10) are considered in equilibrium when there is no velocity gradient ($A = 0$), so that:

$$V_a = aC\frac{\rho_l^{4/15}\sigma^{3/5}C_\mu^{3/10}(\bar{\rho}\widetilde{Y})^{-13/15}}{3\tilde{\epsilon}^{2/5}} \tag{16}$$

where a is given by Eq. (15), C is a constant equal to 0.7 in this study and σ the surface tension coefficient.

Assuming a spherical shape for the droplets, the Sauter Mean Diameter (SMD) can be derived from the mean liquid mass fraction $\widetilde{Y}$ and the mean liquid/gas interface density $\overline{\Sigma}$:

$$\mathrm{SMD} = \frac{6\bar{\rho}\widetilde{Y}}{\rho_l\overline{\Sigma}} \tag{17}$$

3. Numerical procedure

Computations are performed thanks to the CFD code Fluent version 12.1 using User Defined Functions (UDF) to introduce the transport equations for the mean liquid mass fraction and the mean liquid/gas interface density.

Eqs. (1)–(16) are solved using the finite-volume method in association with the SIMPLE algorithm and the Second Order Upwind scheme. The SIMPLE algorithm uses a relationship between velocity and pressure corrections to enforce mass conservation and to obtain the pressure field. Second-order discretization is more accurate and is more suited for complex flows. The standard wall functions are used to model the near-wall region. They give reasonable predictions for the majority of high-Reynolds-number wall-bounded flows.

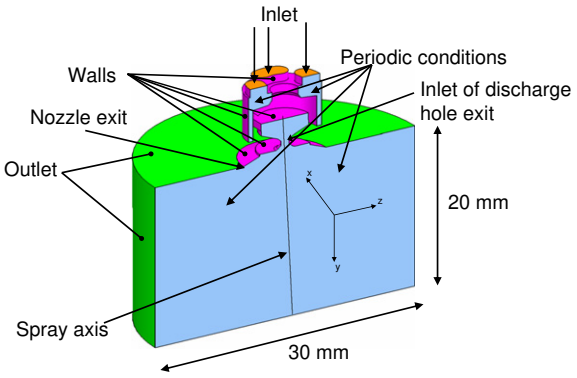

Fig. 1. Geometry and boundary conditions, three-dimensional.

Because the liquid is injected tangentially into the swirl chamber, it is not possible to perform directly two-dimensional calculations in order to compute the flow inside and outside the nozzle with discharge hole exit diameter equal to 0.92 mm. Firstly, three-dimensional calculations are carried out to study the flow of water ($\rho_l = 998.2$ kg/m^3) into air ($\rho_g = 1.225$ kg/m^3) from the inside of the nozzle up to 20 mm outside the exit (see Fig. 1). Viscosity is taken constant and equal to $\mu = 5.1 \times 10^{-5}$ kg/m.s ($\mu = (\mu_{water} + \mu_{air})/2$). The surface tension is that of water, $\sigma = 72$ mN/m. We will introduce, in the second time, the surfactant modifying the value of the surface tension (see Fig. 11, Section 5.1).

There are two parts: a first one (orange and pink) represents the half-nozzle and a second one (green) represents the outlet computational domain attached to the half-nozzle in order to calculate the flow at exit. Outlet computational domain dimensions must be sufficiently large so that the boundary conditions do not influence the flow. The orange parts (Inlet) are the inlet orifices where the liquid is initially injected. The pink parts (Walls) represent the solid walls of nozzle whereas those in green (Outlet) are the outlet. Periodic conditions (blue[1]) are used in order to compute the flow in half domain. The inlet boundary conditions used to perform the calculations are 4 bar for injection relative pressure, 1 for liquid mass fraction, 10% for turbulence intensity defined by $I = \sqrt{\sum_{i=1}^{3} u_i''^2}/\sqrt{\sum_{i=1}^{3}\tilde{u}_i^2}$ and 4 mm for integral turbulence scale corresponding to the diameter of the inlet orifice. The outlet boundary conditions are atmospheric pressure, 10% for turbulence intensity and 2.4 mm for integral turbulence scale, zero diffusive flux for $\widetilde{Y}$ and $\overline{\Sigma}$ if the fluid goes out of the domain, $\widetilde{Y} = 0$ and $\overline{\Sigma} = 0$ if the fluid (gas) goes into the domain. At walls, no slip condition and zero diffusive flux for $\widetilde{Y}$ and $\overline{\Sigma}$ are prescribed. A non-uniform mesh grid composed of 1,800,000 tetrahedral cells is used. Distribution of grid nodes is arranged to ensure that small regions with large gradients are sufficiently resolved. It was refined within the half-nozzle inlet where the grid spacing inside the discharge hole was about 0.03 mm. The mesh is coarser downstream, according to a geometric progression of reason 1.02, to reduce the computational time. The total computational time is of the order of 6 days on an 2.4 GHz Intel Pentium Xeon Processor. Fig. 2a and b present respectively the liquid mass fraction field $\widetilde{Y}$ and the mean

[1] For interpretation of color in Figs. 1, 2, 5–14, the reader is referred to the web version of this article.

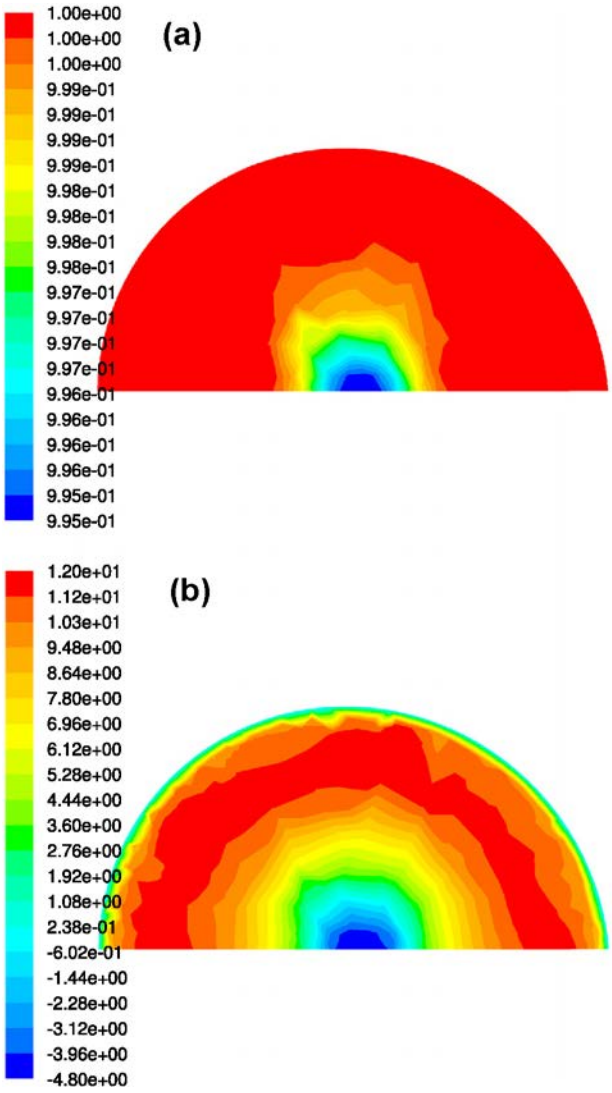

Fig. 2. Fields on the plane located at the inlet of discharge hole exit, perpendicular to the spray axis: (a) Mean liquid mass fraction field (–) and (b) Mean axial velocity field ($m\,s^{-1}$).

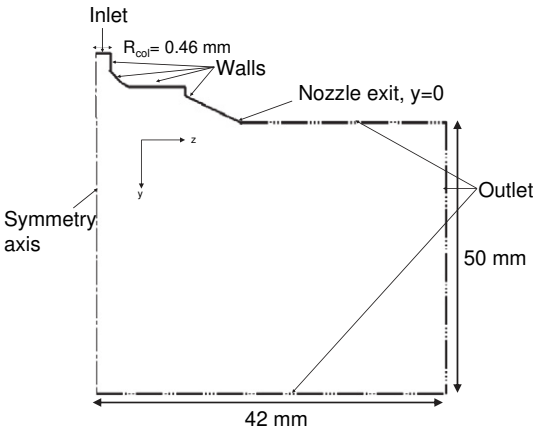

Fig. 3. Geometry and boundary conditions, two-dimensional.

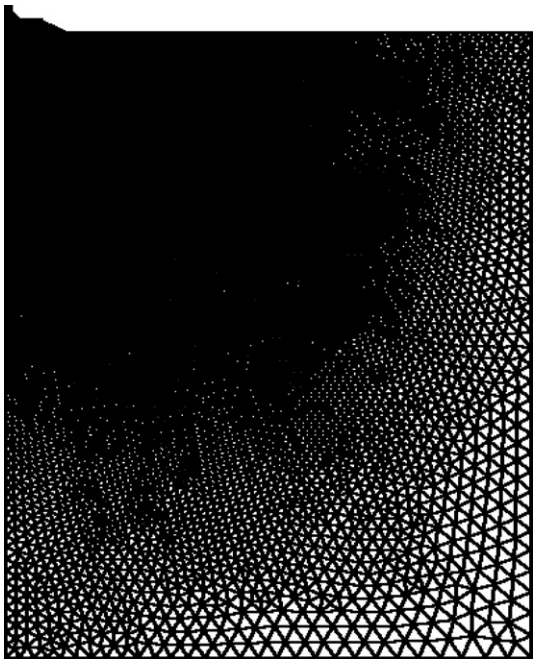

Fig. 4. Schematic of computational grid, two-dimensional.

axial velocity field on the plane located at inlet of discharge hole exit.

The results show that mean liquid mass fraction and mean axial velocity are almost axisymmetric on the plane located at inlet of discharge hole exit. Then, the flow behavior can be assumed as quasi-axisymmetric. In order to decrease computational time and to increase outlet computational domain and because the flow is axisymmetric on the plane located at inlet of discharge hole exit, two-dimensional axisymmetric swirl calculations are, secondly, performed. The restricted area (semi-circular area of 0.92 mm in diameter) of plane located at inlet of discharge hole exit is selected to define the boundary inlet conditions for the two-dimensional axisymmetric swirl calculations. Thus, radial profiles of velocity components, turbulence, mass fraction and liquid–gas interface density are recovered from this area and are used as boundary conditions in the two-dimensional case (see inlet edge of 0.46 mm in radius in Fig. 3). The boundary conditions at outlet and walls are the same as for the three-dimensional case. This new computational domain is bounded from the new inlet to $y = 50$ mm and from the spray axis to $z = 42$ mm along the axial and radial directions respectively (see Fig. 3). A non-uniform mesh grid is composed of 26,000 triangular cells with a grid spacing inside the discharge hole of 0.03 mm (see Fig. 4). Mesh independence tests have been performed to verify the grid independence of model results. The computational time is then just less than one hour. Therefore, the results shown in paragraph 5 are obtained with the two-dimensional approach.

4. Experimental set-up

Water droplets are generated by a swirl nozzle used in agricultural applications (ATR 80 lilas Albuz St Gobain, France). The injection relative pressure of water is 4 bars (flow rate 0.32 l/mn). Hence, the conic hollow core of finely atomized droplets spreads theoretically with a 80°23 angle. Velocity and diameter of droplets are simultaneously measured by Phase Doppler Anemometry with a PDA system (DANTEC Dynamics) (see Fig. 5).

The optical set up consists in a 60 mm emission fiber optic associated to the 514.5 nm wavelength of an Argon ion laser (4 W, Spectra-Physics) which generates the probe volume ($700 \times 80 \times 80\ \mu m^3$). The forward scattered light is collected by a

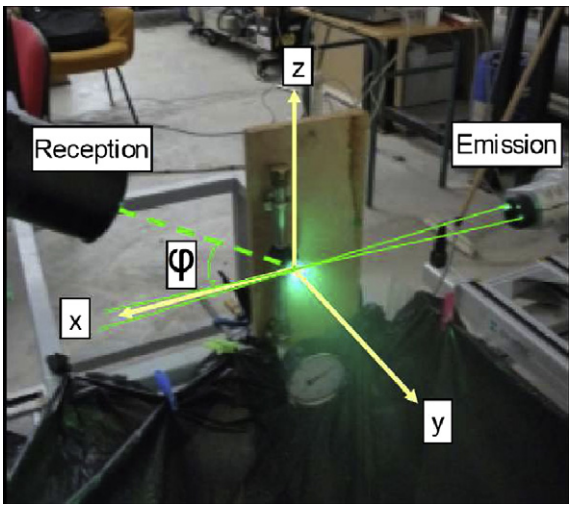

Fig. 5. Experimental set-up for droplet analysis by Phase Doppler Anemometry.

112 mm fiber optic. For water droplets in air, the relative refraction index is $n_{rel} = n_{water}/n_{air} = 1.334$, so that the detection of particles is based on the first order of refraction with a diffusion angle of $\phi = 35°23$ with a parallel polarization. The Doppler signal is analyzed with a BSA P80 associated with the software BSA Flow v4.50. The instantaneous y-component of the velocity and particle diameter are simultaneously measured. The post-process gives the velocity and diameter statistics including the Sauter Mean Diameter (SMD). The droplet cloud is investigated from the exit section up to $y = 30$ mm, both radially and axially (see Fig. 5).

5. Results and discussion

5.1. Modeling results

Fig. 6 presents the mean liquid mass fraction field $\widetilde{Y}$. The mean liquid mass fraction lies between 0 and 1. Value 0 (in blue) represents the air whereas value 1 (in red) represents the liquid. Inside the nozzle, there is only liquid, and, as the liquid penetrates the gas phase, the mean liquid mass fraction in the sheet center decreases. Outside of the spray, there is only air. On the spray axis, the mean liquid mass fraction decreases downstream.

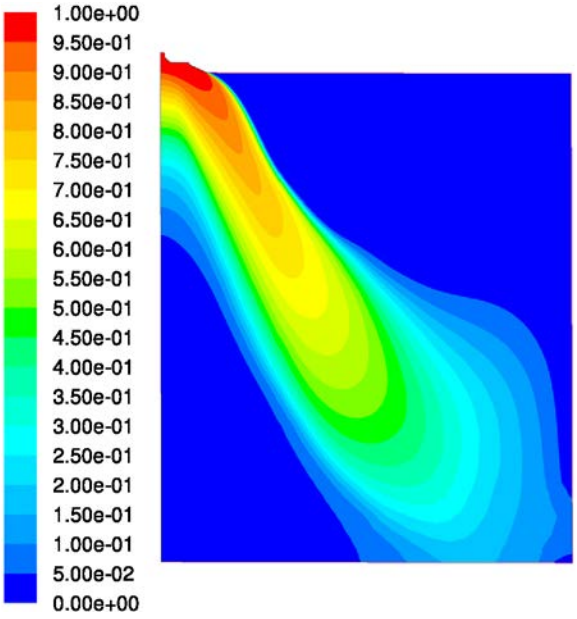

Fig. 6. Field of the mean liquid mass fraction, modeling.

Fig. 7 presents radial profiles of the mean liquid volume fraction $\bar{\tau}$ defined by Eq. (7) at axial positions $y = 1$, 2, 3 and 5 mm from the nozzle exit edge. Hollow cone spray is clearly visible, the minimum values of mean volume fraction are found close to the spray axis (i.e. Radial Position = 0). In the spray center, the non-zero mean volume fraction may represent the volume fraction of the small droplets carried backward by the air flow recirculation.

Predicted radial profiles of diagonal components of Reynolds Stress tensor close to nozzle exit edge ($y = 1$ mm) are plotted in Fig. 8.

Clearly, the maximum value of $\widetilde{u''^2}$ is almost twice larger than the maximum values of $\widetilde{v''^2}$ and $\widetilde{w''^2}$. This result shows that the turbulence is anisotropic and the choice of Reynolds Stress Model is therefore justified. Moreover, other results, not presented here, where the isotropic standard $(\tilde{k}, \tilde{\epsilon})$ model is used, indicated no realistic spray as compared with experimental data on hollow-cone sprays (Belhadef, 2010).

The injection pressure influence has been tested by modifying the initial value from 4 bars to 8 bars (Figs. 9 and 10).

The injection pressure recommended by manufacturers with this type of nozzle varies between 3 and 15 bars. These two values (4 and 8 bars), in this study, correspond to those usually used for

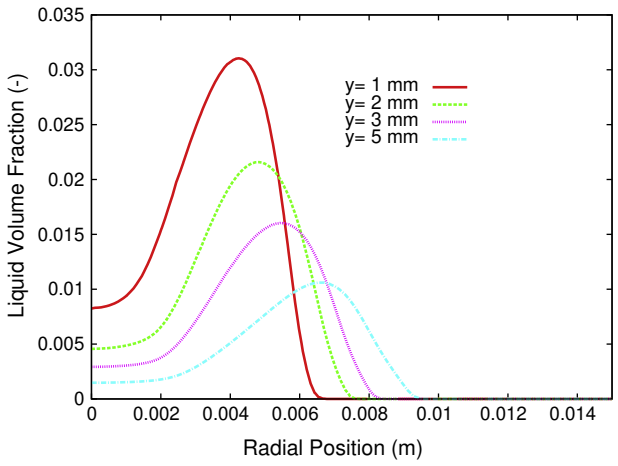

Fig. 7. Radial profiles of the mean liquid volume fraction, modeling.

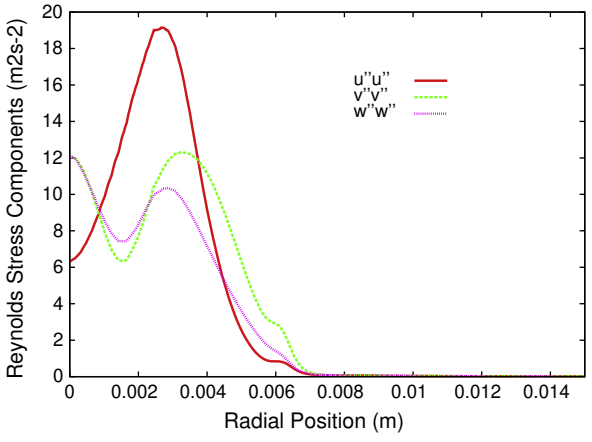

Fig. 8. Radial profiles of diagonal components of Reynolds stress tensor at $y = 1$ mm, modeling.

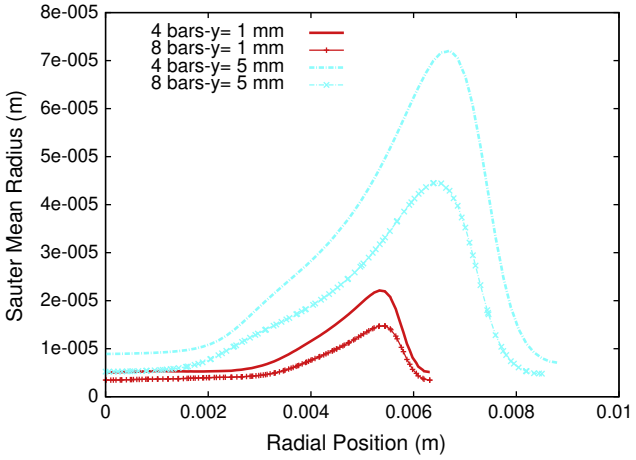

Fig. 9. Radial profiles of Sauter Mean Radius for two injection pressure values at $y = 1$ mm and $y = 5$ mm, modeling.

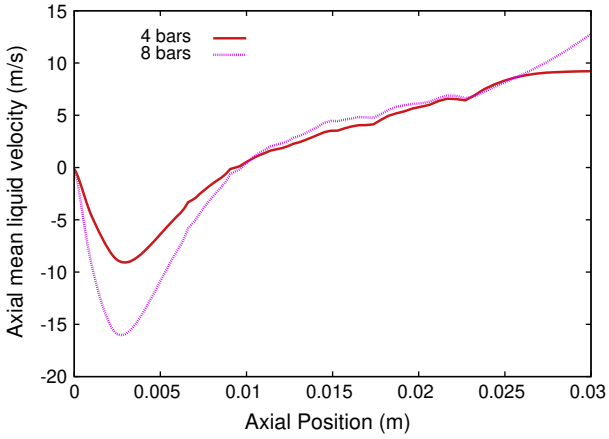

Fig. 10. Axial profile of the axial mean liquid velocity for two injection pressure values, modeling.

agricultural applications. The Sauter Mean Radius decreases by increasing injection pressure value (Fig. 9). This can be explained as higher injection pressure leads to higher velocity of liquid sheet and causes reduction of the drop size.

It should be recalled that modeling mean velocity is a mean velocity for the mixture ($\tilde{u}$), whereas the measured mean velocity corresponds to the liquid velocity only ($\overline{u_l}$). Nevertheless, the mean liquid velocity can be calculated from the mixture mean velocity and according to the liquid diffusion turbulent flow $\bar{\rho}\widetilde{u_i''Y''}$ (Demoulin et al., 2007).

$$\bar{u}_{i/l} = \tilde{u}_i + \frac{\bar{\rho}\widetilde{u_i''Y''}}{\bar{\rho}\tilde{Y}} \tag{18}$$

Therefore, the axial component of this mean liquid velocity will be compared for two injection pressure values, 4 and 8 bars (Fig. 10).

The recirculation zone remains almost constant with increasing injection pressure (Fig. 10). However, the higher injection pressure leads to higher magnitude axial mean velocity of liquid sheet. The maximum value of magnitude axial mean liquid velocity equals 16 m/s for 8 bars and 9 m/s for 4 bars.

The surface tension coefficient of the water–air is 72 mN/m. In agricultural spraying, the surfactant is mixed with water at concentrations recommended by manufacturers. The principal role of surfactant is to reduce the surface tension coefficient in order to

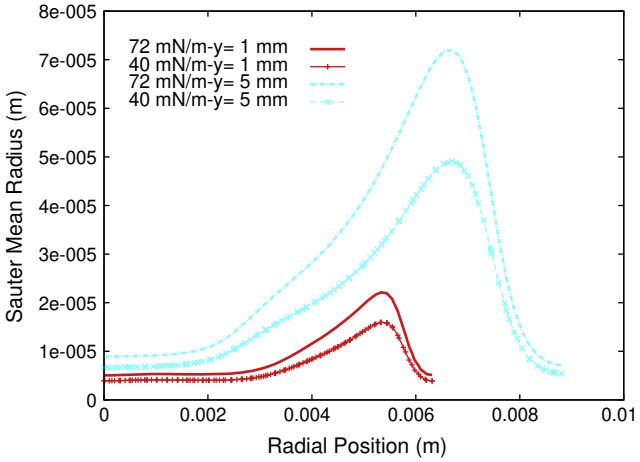

Fig. 11. Radial profiles of Sauter Mean Radius for two surface tension coefficient values at $y = 1$ mm and $y = 5$ mm, modeling.

enhance the spreading out of the drops on the targeted leaves and to avoid the rebound. Fig. 11 gives the radial profiles of Sauter Mean Radius for two surface tension coefficient values: 72 mN/m (water–air) and 40 mN/m (surfactant added to water–air). Note that the surface tension coefficient appears in the destruction term of the mean liquid/gas interface density (see Eq. (16)). Reduction of the surface tension coefficient causes destruction reduction of the mean liquid/gas interface density and consequently a reduction in the Sauter Mean Radius of the drops. The results shown on Fig. 11 confirm this assumption where the Sauter Mean Radius is weaker with a weaker surface tension coefficient.The addition of the surfactant leads to produce more interfaces but has an adverse effect hoped since the formed drops are smaller and thus more sensitive to the drift.

5.2. Comparison with experimental results

Fig. 12 shows comparison of axial profiles of the axial mean liquid velocity obtained on the spray axis both experimentally and by modeling.

Good agreement between predictions and measurements is generally found. Note that axial mean liquid velocity has negative values from the nozzle exit up to, 11 mm for PDA, and 10 mm for model. Indeed, the annular configuration is responsible for the formation of a recirculation zone just after the nozzle exit (Siamas et al., 2009).

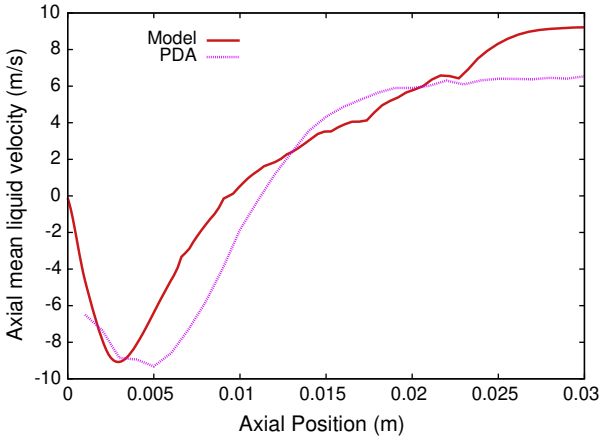

Fig. 12. Axial profile of the axial mean liquid velocity, modeling and experimental comparison.

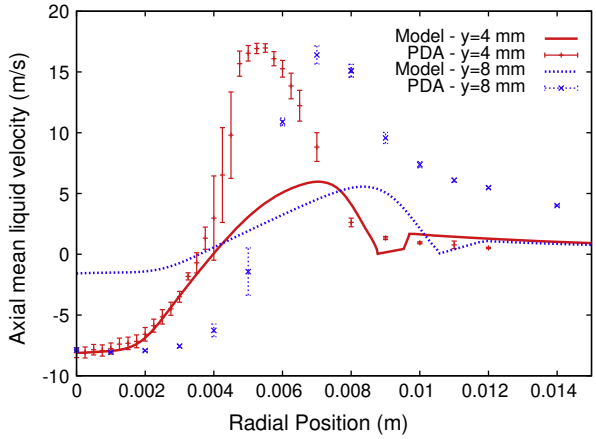

Fig. 13. Radial profile of the axial mean liquid velocity, modeling and experimental comparison.

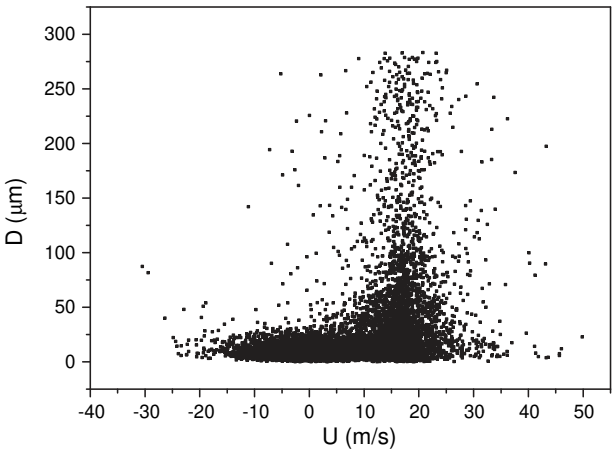

Fig. 15. Instantaneous droplet velocity and diameter for radial position = 4 mm at $y = 4$ mm.

Fig. 13 presents a comparison between radial profiles of the modeling and experimental axial mean liquid velocity at axial positions $y = 4$ mm and 8 mm from the nozzle exit edge. The axial mean liquid velocity calculated by the model presents a maximum of approximately 6 m/s whereas in experiments, the axial mean liquid velocity has a maximum close to approximately 15 m/s. The liquid sheet calculated by the model is broader. Therefore, to preserve the mass flow rate, it is necessary that the axial mean liquid velocity given by the model is lower.

Fig. 14 presents a comparison of radial profiles of the modeling and experimental Sauter Mean Diameter at axial positions $y = 4$ mm and 8 mm from the nozzle exit edge.

Close to the spray axis (i.e., Radial Position = 0) where the liquid volume fraction is weak (see Fig. 7), small drops with SMD bounded between 10 and 30 μm are observed. In addition, good agreement between predicted and measured SMD is found in the liquid sheet (i.e., 0.003 m $\leqslant$ Radial Position $\leqslant$ 0.009 m). Outside of the spray (i.e., Radial Position > 0.008 m for $y = 4$ mm and Radial Position > 0.01 m for $y = 8$ mm), the liquid volume fraction tends towards 0 and the mean liquid/gas interface density $\overline{\Sigma}$ does not have any physical significance in this zone. Therefore, the SMD calculated by the model will not be presented in this zone. However, the SMD measured by the PDA, in this zone, varies between 25 μm at $y = 4$ mm and 50 μm at $y = 8$ mm.

Fig. 15 presents instantaneous droplet velocity and diameter for Radial Position = 4 mm at $y = 4$ mm measured by PDA. In the internal region of the droplet sheet, the PDA detects two populations of droplets. One population is composed of small droplets with diameter inferior to 20 μm coming from downstream with a negative velocity. This observation is in agreement with the commented result on the mean liquid volume fraction prediction given in Fig. 7. The second population is representative of larger droplets which follow the sheet development with a positive velocity around 15 m/s. Few droplets of diameter larger than 150 μm contribute significantly to the SMD estimation, although they are not frequently encountered in the droplet population. The error bars presented on PDA measurements take into account the bias introduced by these large particles in the experimental SMD calculation.

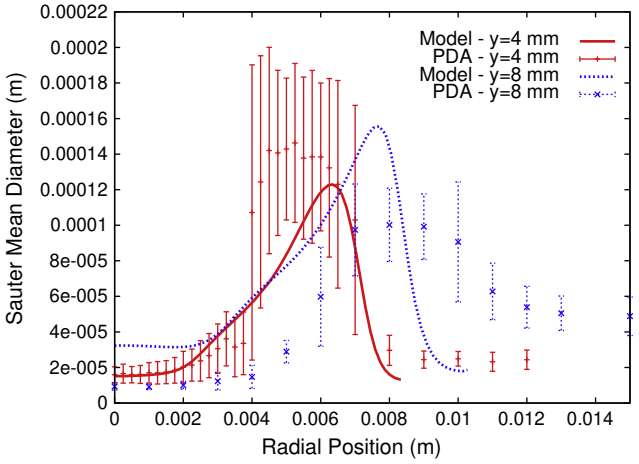

Fig. 14. Radial profile of the Sauter Mean Diameter (SMD), modeling and experimental comparison.

6. Conclusion

Modeling and experimental studies are carried out to examine pressure-swirl atomization. Results concerning axial mean liquid velocity profiles on the spray axis and at various axial positions show good accordance: magnitude orders and the recirculation zone length are comparable. Equation of the mean surface area of the liquid–gas interface per unit of volume $\overline{\Sigma}$ is developed to obtain droplet diameter. Modeling results indicate the formation of a hollow conical spray made up of large droplets and the presence of a recirculation zone close to the spray axis made up of small droplets, in accordance with the experimentation. Comparison of the Sauter Mean Diameter (SMD) calculated by the model and measured in experiments by Phase Doppler Anemometry (PDA) shows good agreement. Moreover, the model will be improved to have better agreement with experimental axial mean liquid velocity. The closure for the liquid turbulent flux $\widetilde{\rho u_i'' Y''}$ could be calculated using a transport equation in order to take into account the gradients of the mean velocity and of the pressure.

References

Belhadef, A., 2010. Contribution à la modélisation Eulérienne de l'atomisation pour la pulvérisation agricole. PhD thesis, Cemagref, Université de Provence, Marseille, France.

Chang, K.C., Wang, M.R., Wu, W.J., Hong, C.H., 1993. Experimental and theoretical study on hollow-cone spray. J. Propul. Power 9, 28–34.

Chigier, N.A., Beer, J.M., 1964. Velocity and static pressure distributions in swirling air jets issuing from annular and divergent nozzles. J. Basic Eng., 788–796.

Demoulin, F.X., Beau, P.A., Blokkeel, G., Mura, A., Borghi, R., 2007. A new model for turbulent flows with large density fluctuations: application to liquid atomization. Atomization Sprays 17, 315–345.

De Luca, M., Vallet, A., Borghi, R., 2009. Pesticide atomization modeling for hollow-cone nozzle. Atomization Sprays 19, 741–753.

Drew, D.A., 1983. Mathematical modelling of two-phase flow. Annu. Rev. Fluid Mech. 15, 261291.
Fu, S., Launder, B.E., Leschziner, M.A., 1987. Modeling strongly swirling recirculating jet flow with Reynolds-stress transport closures. In: Sixth Symposium on Turbulent Shear Flows.
Gibson, M.M., Launder, B.E., 1978. Ground effects on pressure fluctuations in the atmospheric boundary layer. J. Fluid Mech. 86, 491–511.
Hirt, C.W., Nichols, B.D., 1981. Volume of fluid (VOF) method for the dynamics of free boundaries. J. Comput. Phys. 139, 201225.
Ishii, M., 1975. Thermo-fluid dynamic theory of two-phase flow. NASA STI/Recon Technical Report A, 75.
Launder, B.E., Spalding, D.B., 1972. Lectures in Mathematical Models of Turbulence. Academic Press, London, England.
Lebas, R., Menard, T., Beau, P.A., Berlemont, A., Demoulin, F.X., 2009. Numerical simulation of primary break-up and atomization: DNS and modelling study. Int. J. Multiphase Flow 35, 247–260.
Lin, J., Qian, L., Xiong, H., Chan, T.L., 2009. Effects of operating conditions on droplet deposition onto surface of atomization impinging spray. Surf. Coat. Technol. 203, 1733–1740.
Luret, G., Menard, T., Berlemont, A., Reveillon, J., Demoulin, F.X., Blokkeel, G., 2010. Modeling collision outcome in moderately dense sprays. Atomization Sprays 20, 251–258.
Melese Endalew, A., Debaer, C., Rutten, N., Vercammen, J., Delele, M.A., Ramon, H., Nicolaï, B.M., Verboven, P., 2010. Modelling pesticide flow and deposition from air-assisted orchard spraying in orchards: a new integrated CFD approach. Agri. Forest Meteorol. 150, 1383–1392.
Moona, S., Abo-Serie, E., Bae, C., 2009. Air flow and pressure inside a pressure-swirl spray and their effects on spray development. Exp. Therm. Fluid Sci. 33, 222–231.
Nonnenmacher, S., Piesche, M., 2000. Design of hollow cone pressure swirl nozzles to atomize newtonian fluids. Chem. Eng. Sci. 55, 4339–4348.
Osher, S., Sethian, J.A., 1988. Fronts propagating with curvature-dependent speed: algorithms based on Hamilton-Jacobi formulations. J. Comput. Phys. 79, 1249.
Park, H., Heister, S.D., 2006. Nonlinear simulation of free surfaces and atomization in pressure swirl atomizers. Phys. Fluids 18.
Park, H., Yoon, S.S., Heister, S.D., 2006. On the nonlinear stability of a swirling liquid jet. Int. J. Multiphase Flow 32, 1100–1109.
Ponstein, J., 1959. Instability of rotating cylindrical jets. Appl. Sci. Res. 8, 425–456.
Rho, B.J., Kang, S.J., Oh, J.H., Lee, S.G., 1998. Swirl effect on the spray characteristics of a twin-fluid jet. KSME Int. J. 12, 899–906.
Rizk, N.K., Lefebvre, A.H., 1985. Internal flow characteristics of simplex swirl atomizers. J. Propul. Power 1.
Siamas, G.A., Jiang, X., Wrobel, L.C., 2009. Dynamics of annular gas–liquid two-phase swirling jets. Int. J. Multiphase Flow 35, 450–467.
Vallet, A., Burluka, A.A., Borghi, R., 2001. Development of a Eulerian model for the atomization of a liquid jet. Atomization Sprays 11, 619–642.
Xiong, H.B., Lin, J.Z., Zhu, Z.F., 2009. Three-dimensional simulation of effervescent atomization spray. Atomization Sprays 19, 75–90.
Yang, J.T., Chen, A.C., Yang, S.H., Huang, K.J., 2003. Flow analysis of spray patterns of pressure-swirl micro atomizers. In: Proceedings of Pacific Symposium on Flow Visualization and Image Processing. Chamonix, France.